Electrochimica Acta 444 (2023) 142017

Contents lists available at ScienceDirect

Electrochimica Acta

journal homepage: www.journals.elsevier.com/electrochimica-acta

Determining the proton diffusion coefficient in highly hydrated iridium oxide films by energy dispersive X-ray absorption spectroscopy

Elisabetta Achilli [a], Simone Minelli [b], Irene Casale [b], Xiufang He [b], Giovanni Agostini [c], Giorgio Spinolo [d], Paolo Ghigna [d,*], Alessandro Minguzzi [b,e,*], Alberto Vertova [b]

[a] Diparimento di Tecnologie di Generazione e Materiali, Ricerca sul Sistema Energetico - RSE S.p.A., via V. Callegari, Piacenza 29122, Italy
[b] Dipartimento di Chimica, Università degli Studi di Milano, Via Golgi 19, Milan 20133, Italy
[c] ALBA Synchrotron Light Source, Carrer de la Llum 2-26, Cerdanyola del Vallès, Barcelona, Spain
[d] Dipartimento di Chimica, Università degli Studi di Pavia, Via Taramelli 16, Pavia 27100, Italy
[e] Dipartimento di Energia, Politecnico di Milano, Via Lambruschini, 4a - 20156 Milano

ARTICLE INFO

Keywords:
Oxygen evolution reaction
Electrochemical impedance spectroscopy
Warburg element
EIROF

ABSTRACT

Charge transfer reactions in electrodeposited iridium oxide films (EIROF) are investigated by means of operando energy dispersive X-ray absorption spectroscopy (EDXAS), where oxidation and reduction conditions are selected to drive the Ir(III)/Ir(IV) and Ir(IV)/Ir(V) reactions in acidic solutions. The Ir(III)/Ir(IV) couple is related to a well-known electrochromic phenomenon, while the Ir(IV)/Ir(V) couple might play an important role in the catalysis of the oxygen evolution reactions (OER). In the experiments, current intensity and time-resolved X-ray absorption spectroscopy (XAS) are simultaneously recorded upon application of appropriate potential steps, leading to the independent determination of both the relevant reaction rates and the rate-determining steps. This is allowed by the fast acquisition time ($\sim 10^{-2}$ s) at the ESRF Energy Dispersive XAS (EDXAS) ID24 beam-line, in combination with the highly hydrated amorphous iridium oxide electrode material, which in turn allows to maximize the fraction of Ir sites participating in the electrochemical processes. If the experimental conditions exclude the possibility of having either oxygen evolution (or reduction), the Degree of Reaction (DoR), determined by both electrochemistry and XAS, exhibits exponential time dependence, clearly pointing to diffusion-controlled processes. *Vice versa*, under concomitant OER + oxidation of iridium centers or ORR + iridium reduction, the electrochemical and XAS DoRs highlight different phenomena, providing fully complementary information of the ongoing electrode reactions. In all cases, data elaboration allows to determine the diffusion coefficient of H^+ ions within the catalyst layer, that is compared and confirmed by data obtained by electrochemical impedance spectroscopy (EIS). The high values of *D* obtained for EIROF is compared to values obtained on other IrO_2 materials can help in explaining the relevant high electrocatalytic activity.

1. Introduction

Highly hydrated iridium oxide films (namely, electrodeposited iridium oxide films, EIROFs) have been often adopted in the studies devoted to the disclosure of the OER mechanism, both in electrochemical [1,2] and photo-electrochemical water splitting [3,4] as well as for super-capacitors and pH sensors [5]. Iridium oxide is the benchmark for OER in both acidic and alkaline solutions [6–11], for the oxygen reduction reaction (ORR) [12], and is one of the most used anode materials in the electrochemical industrial processes [13–15], like cathodic protection [16] and metal electro-winning [17].

EIROF [18,19] represent one of the best playground for combined spectro-electrochemical investigations, thanks to their high degree of hydration which favors ion intercalation/deintercalation(*e.g.* H^+, OH^-). This determines the availability of a high concentration of easy accessible electrochemically active sites: all the Ir present in the layer is electrochemically active [20]. Moreover, highly defective, amorphous electrochemical oxides (including EIROFs) shows a remarkable activity, accompanied by a reduced stability compared to thermally-prepared IrO_2 electrodes [21–23].

EIROF, and in general, oxide electrodes under OER undergo solid-state redox processes according to the sequence “higher valence oxide

* Corresponding authors.
E-mail addresses: paolo.ghigna@unipv.it (P. Ghigna), alessandro.minguzzi@unimi.it (A. Minguzzi).

https://doi.org/10.1016/j.electacta.2023.142017
Received 30 December 2022; Received in revised form 31 January 2023; Accepted 5 February 2023
Available online 7 February 2023
0013-4686/© 2023 Published by Elsevier Ltd.

formation/higher valence oxide decomposition", as described by reactions (1) and (2):

Higher valence oxide formation:

$$MO_x + H_2O \rightarrow MO_{x+1} + 2H^+ + 2e^- \quad (1)$$

Higher valence oxide decomposition:

$$MO_{x+1} \rightarrow MO_x + \frac{1}{2}O_2 \quad (2)$$

Note that reaction (1) is a specific version of the so-called generalized pseudo-capacitive reaction (3):

$$MO_x(OH)_y + \delta H^+(\text{solution}) + \delta e^-(\text{oxide}) \rightleftarrows MO_{x-\delta}(OH)_{y+\delta} \quad (3)$$

In the case of iridium oxide, reaction (3) has been deeply studied [18] because of the electrochromic effect that accompanies the intercalation/deintercalation of H^+ upon reduction/oxidation of the metal centers. In fact, upon application of the appropriate potentials, iridium oxide switches forth and back between the highly resistive and transparent oxide of Ir(III) and the highly conductive oxide of Ir(IV), with a good retention of the optical features (color), provided that the layer preserves a high hydration degree.

Here we assume that, for reactions 1-3, the charge is balance solely by H^+, since the present study is carried out in aqueous H_2SO_4. However, it is worth noting that the relevant anion can take part at the reaction [10,24], most likely decreasing the mobility of protons.

Reaction (3) can be safely defined as a reference method for determining the active area of oxides electrodes [25,26]: the number of sites available for pseudo-capacitance charge/discharge can be easily counted [10,27] and is proportional to the number of active sites for other reactions, if both kinds of process imply the exchange of the same ion.

Nonetheless, as initially evidenced by Trasatti [28], not all sites are equally accessible for ion exchange with the electrolyte. The coexistence of sites with different accessibility can have huge effects on the final behavior of the catalyst and, most of all, on the comparison of different catalysts with the aim of inferring intrinsic activities from the experimental results.

In more detail, it is found that the integrated voltammetric charge in the pseudocapacitive region does not depend linearly on the potential scan rate [29]. Later, Ardizzone and Trasatti involved a "slow access of protons to "inner" regions of the surface" and showing an inversely proportion between the charge and the square root of the scan rate, suggesting that a semi-infinite diffusion might be at the bases of this phenomenon [30].

More recently, several reports highlighted the role of surface –OH groups (and their coverage) as a useful descriptor for the activity and stability of the material [31]. In addition, "hydration" and proton diffusivity are most likely correlated, being H^+ diffusion due to its hopping between water molecules (Grotthus mechanism) and considering the most recent observations that demonstrates the formation of $H_7O_3^+$ as the core/inner unit of any hydrated proton resulting from the strong interaction between an H^+ ion and three water molecules [32].

These reports suggest that the diffusion of proton into oxide-based electrocatalysts plays a key role in the final performance of the material and, therefore, that we should better investigate on it.

A challenging problem in the study of heterogeneous catalysis is the presence of a multiplicity of active surface sites showing an "average" behavior that is difficult to treat and analyze for obtaining mechanistic insights. *Vice versa*, in homogeneous catalysis the knowledge of the exact chemical nature of the initial state is generally available and makes the understanding of the overall catalytic cycle easier.

In electrocatalysis, the kinetic information on the heterogeneous electron and charge transfers are embedded in the potential/current relationships, representing powerful tools [33] for analyzing possible reaction paths and the role of the active surface sites. Nonetheless, the combination of electrochemical and spectroscopic techniques offers unique potentialities for elucidating the role of the electrocatalyst and the effectiveness of the matrix [34]. In particular, XAS provides key information on the electronic structure and the charge state of the photo-absorber, switching on a powerful floodlight on the role of the electrode material under operating conditions [35,36].

Notwithstanding the "high gain" features of this combined spectro-electrochemical technique, both (i) the surface to mass ratio of the electrocatalyst and (ii) the time and energy resolution of the XAS signal must be maximized to fully exploit the potentialities of hard and highly penetrating X-rays towards the investigation of time dependent interfacial phenomena. This implies (i) choosing sound protocols for preparing and depositing the active material, and (ii) appropriately selecting the perturbation signal(s) and the relevant time domain(s). Although the current itself intrinsically carries the key information on the kinetics of the electrochemical reaction, under most of the actual conditions, *e.g.* in presence of concurrent/parallel/side reactions, at least another independent, time-resolved determination is necessary to obtain reliable mechanistic insights.

This shifts the attention towards the time resolution of the classical XAS experiment, either in transmission or fluorescence mode, where the limitation arises from the time needed for the monochromator to scan over the desired energy range. Rapid scanning monochromators can considerably reduce the time needed to register a spectrum by employing a continuous rotation of the monochromator. In this technique, called QUICK-XAS [37] a whole XAS spectrum can be collected in seconds or fractions of seconds. With this setup, however, the time resolution is generally too low to study the kinetics of multistep electrode processes [25,38]. Improved time resolutions can be obtained by high intensity focused X-ray beams less than 20 μm wide. In the appropriate setup, known as *energy dispersive* XAS (EDXAS), a poly-chromator crystal focuses onto the sample a *polychromatic* beam, which is afterwards dispersed onto the detector. The main downside of *dispersive* XAS relies in its low energy resolution. In addition, it can be used only for transmission experiments, which greatly affects the cell design and the choice of the structural materials, to avoid undesired beam attenuation. So far, the number of time-resolved XAS studies in electrochemistry is rather small [39–43].

Here, we show that time-resolved EDXAS, being an element selective technique and allowing operando experiments, is capable of directly monitoring the pseudo-capacitive event and thus pointing out (and quantifying) the accessibility of sites in the model system. We proved that the analysis of *operando* XAS spectra recorded during well-defined stages of a pseudo-capacitive event allows to highlight structural modifications of the active sites of the material [44]. In this work we approach the time evolution of the reaction by analyzing simultaneous chronoamperometry and EDXAS at the Ir-L_{III} edge. We demonstrate that the rate determining step of the reactions is the diffusion of H^+ in and out of the EIROF layer. To reach this conclusion, we re-examin the diffusion geometry for a porous layer and use the explicit solution of the Fick laws for this case.

In summary, the present work investigates the behavior of EIROF in acidic media, the condition in which IrO_2 (together with RuO_2) has been for long considered as the only active and stable OER electrocatalyst. We evidence the need of optimal experimental conditions for both electrochemistry and XAS set-ups. This implies: (i) stable enough electrodes to sustain the irradiation by a high intensity X-ray beam for a few minutes; (ii) appropriate cell and electrode design for sound and simultaneous *I/E* plus transmission mode-XAS signals acquisition; and (iii) synchronization of the overall measurement chain.

The effectiveness of the method is confirmed by comparison with the results obtained by electrochemical impedance spectroscopy (EIS), a technique that has been previously used for determining ion diffusion in solids, but that suffers for the partial arbitrariness of the choice of the equivalent circuits (more circuits can well-fit the same dataset), that requires steady state conditions (except for dynamic EIS [45]). For these reasons, EIS results should be validated by other techniques to provide reliable results. In this optics, the present work can be also considered as

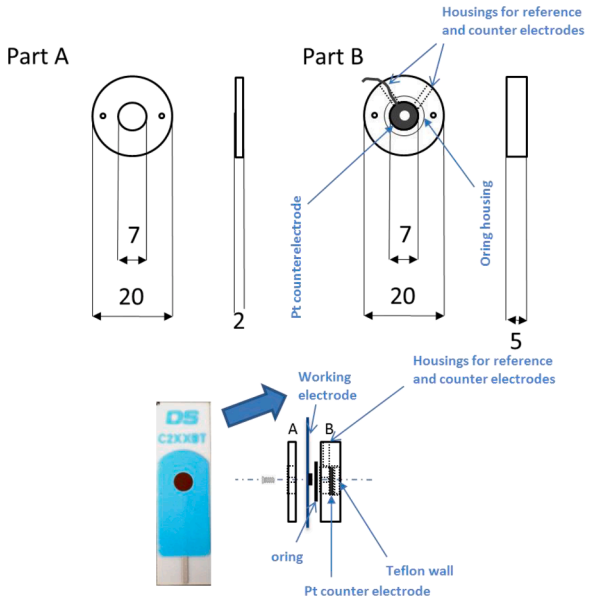

Fig. 1. Scheme of the cell used in this work. Quotes are in mm.

the validation of the use of EIS and of a Randles circuit for the determination of the diffusion coefficient of ions in oxide electrodes.

Compared to other types of IrO_2, EIROF shows a particularly high diffusion coefficient, that certainly contributes to fast bulk mass transport of charges and thus to high electrocatalytic activity, particularly at high current densities.

2. Experimental section

All reagents are used as received and all solutions prepared with Milli-Q grade water. Potentials are referred to the reversible hydrogen electrode, RHE.

2.1. Preparation of working electrodes

The Electrodeposited Iridium Oxide Films (EIROF) are prepared following a modified version of the procedure reported previously [18–20]: 0.0151 g of $IrCl_3 \bullet 3H_2O$ (Alfa Aesar) are dissolved in Milli-Q water (10 ml). After 30 min stirring, 100 µl of H_2O_2 (30%) are added and the resulting solution is kept under stirring for 30 min. Then, 0.0518 g of oxalic acid are added. The solution is stirred for 10 min. Finally, dried K_2CO_3 is added until pH is about 10.5. The procedure leads to the formation of a yellow solution that turns blue/violet after 3 days at room temperature.

The blue colloid is used as a deposition bath, from which IrO_x is easily deposited onto a conductive support (a carbon disk deposited onto a 175 µm thick Polyethylene terephthalate lamina, supplied as a custom electrode by Dropsens) at constant current density. We obtained durable deposits suitable for XAS measurements by applying a 0.1 $mA \bullet cm^{-2}$ current for 8h, using a Pt plate as the counter electrode.

The electrode thickness was determined from the X-ray absorption of the film at 11.215 keV, which gives the product of the absorption coefficient μ by the thickness τ. Then, by measuring the deposit density with a helium pycnometer we can determine μ, and therefore obtain the thickness τ. This results in an average thickness of 300 μm. Assuming that the deposit is homogeneous and considering that the diffusion coefficient is an intensive parameter, we can extend the results obtained in the present paper also to other thicknesses.

2.2. Electrochemical impedance spectroscopy

EIS spectra have been registered between 10^6 and 10-2 Hz with an AC amplitude of 7mV in a standard three compartment cell, using with a Pt foil as counter electrode and SCE with a 0.1µF condenser connected in parallel as reference. The latter was added for avoiding artifacts at high frequencies when experiments are carried out with a high conductivity electrolyte and due to the high impedance of the reference electrode and the cable capacitance [46].

All measurements have been performed with Solartron 1287 and 1260 instrument supported by CorrWare and zPlot and elaborated with zView, version 3.5i.

2.3. Spectro-electrochemical cell

The cell is made of polytetrafluoroethylene (PTFE) and contains a Pt foil counter-electrode and an AgCl/Ag in 0.1 M KCl reference electrode. The electrolyte solution is 0.5 M aqueous H_2SO_4.

The reference electrode is in contact with the solution *via* a salt bridge, consisting in a glass pipette filled with agar containing 0.2 M aqueous $KClO_4$. One side of the cell includes a hole that matches with the WE area. The WE is held between the PTFE cell and a polypropylene plate that also include a hole for the X-rays beam.

All electrochemical and operando XAS experiments were carried out using a CH Instrument 633D potentiostat, driven by the proprietary software.

A scheme of the cell is reported in Fig. 1.

2.4. Energy dispersive-XAS experiments

EDXAS data were collected at ID24 beam-line [47,48] of the European Synchrotron Radiation Facility, ESRF, Grenoble (the ring energy was 6.0 GeV and the ring current 150-200 mA). The X-ray source consisted of two undulators whose gaps were adjusted to tune constant counts of the first harmonic for energies around the Ir L_{III}-edge along the spectra. The beam was focused horizontally by a curved Si(111) polychromator crystal in Bragg geometry and vertically with a bent Si mirror at a glancing angle of 2.5 mrad with respect to the direct beam. The beam size at the sample was 8 μm FWHM horizontally and 80 μm FWHM vertically to decrease the photon density to preserve the samples from beam damaging.

Spectra were recorded in transmission mode using a FreLonCCD camera detector [49]. The energy calibration was made by measuring the absorption spectrum of a Pt foil (Pt-L_{III}: 11564 eV; Ir-L_{III}: 11215 eV).

Sequences of spectra were acquired while applying to the WE selected potential steps and recording the relevant chronoamperometries. Usually, oxidative and reductive potential steps are coupled in sequence. In all cases, the WE is kept at the initial potential for at least three minutes to allow all the sites to assume initial stationary conditions. Afterwards, the potential is set to its final value, at which the spectra are collected. The potential step is triggered by the X-ray acquisition system. All measurements were carried out at room temperature. A sequence is made of 10000 or 20000 spectra acquired every 0.0116 s, that is for a total time of 116 or 232 s. Averages were calculated every 10 spectra in order to obtain a better signal to noise ratio: this gave a final time resolution of 0.116 s.

2.5. Data processing and analysis

Chronoamperometric runs consist in applying to the WE a potential step, $\Delta E = E_f - E_i$, and measuring the cell current, I, as a function of time. For a potential step, the total current flowing into the circuit is

$I = I_c + I_f$, where I_c is the non-faradaic contribution of double-layer charging and I_f is the sought term related to the electron transfer process.

The subtraction of I_c has been described in our previous work [42] and implies the determination of the uncompensated resistance, R_u, that

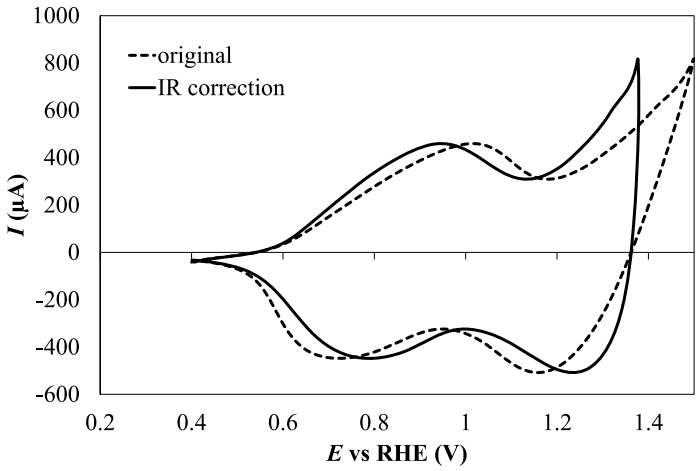

Fig. 2. CV of IrO_x electrode in 0.5 aqueous H_2SO_4 at 2 mV•s^{-1}: original data (dashed line), corrected for the uncompensated ohmic drop R_u = 150 Ω (full line).

was then used to correct the voltammetry shown in Fig. 2.

The raw XAS spectral data were processed with a preliminary stage, in which spectra were normalized, and a subsequent analysis aimed at extracting the kinetic parameters of the processes.

In the preliminary stage, each XAS spectrum of each sequence was normalized by means of the PRESTO PRONTO software [50]. The normalization was made by (i) fitting the pre-edge and post-edge parts of the spectrum with a straight line and a cubic function, respectively; and (ii) rescaling the whole spectrum to unit step in the absorption coefficient at the edge. The same pre-edge and post edge fitting functions were used for all spectra of a sequence.

The analysis stage was in turn based on three major steps: (i) fit of each normalized spectrum of a whole sequence to a simplified spectral model, (ii) calculation of the Degree of Reaction (DoR) from the spectral parameters, and (iii) assessment of a kinetic law from the time evaluation of the DoR along the sequence. The fitting step of the data analysis was carried out by means of the MINUIT program [51], a well-known tool for function minimization and error analysis, writing a subroutine for a multi-parameter function to be optimized. The Ir L_{III}-edge spectrum can be modelled by means of a Lorentzian function, which accounted for the transitions from the initial 2*p* states to the empty 5*d* states, and an arctangent function, accounting for the transition to continuum states.

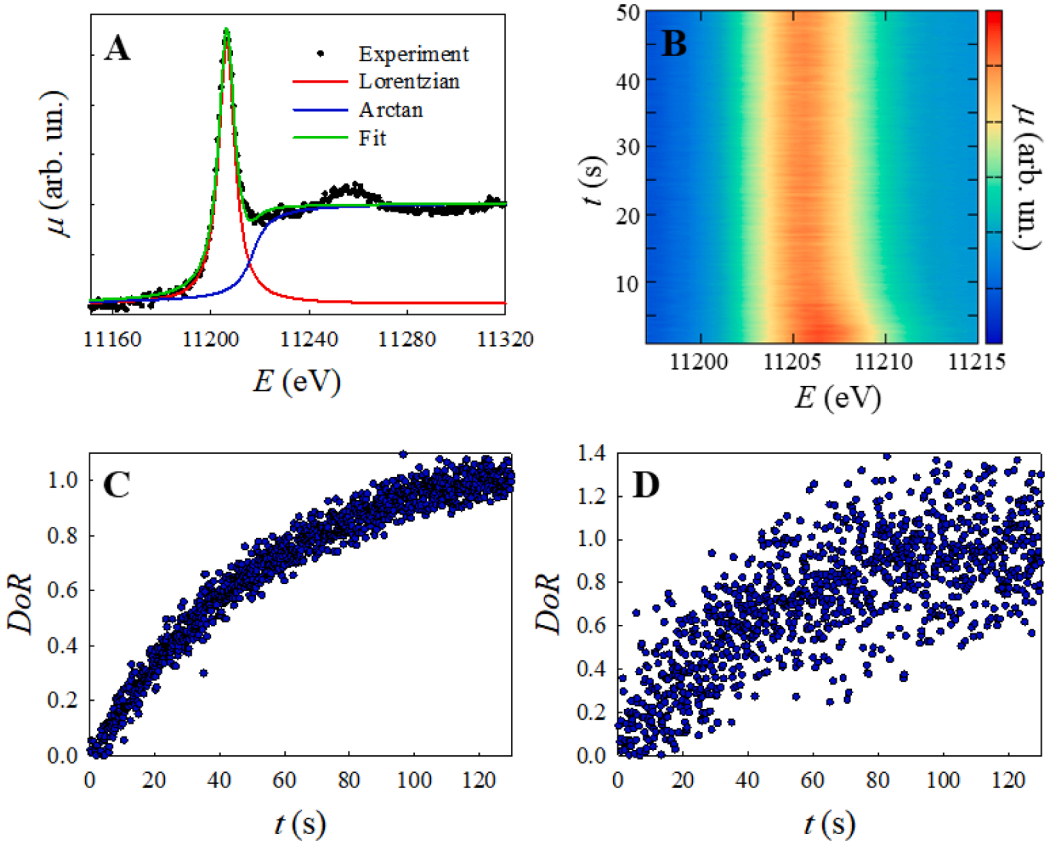

Fig. 3. XAS at the Ir-L_{III} edge. **A**: raw spectrum and fit according to the model described in the text. **B**: contour plot evidencing the time evolution of the spectra. **C**: time evolution of the *DoR* obtained from the energy position of the Lorentzian component. **D**: time evolution of the *DoR* obtained from the width of the Lorentzian component.

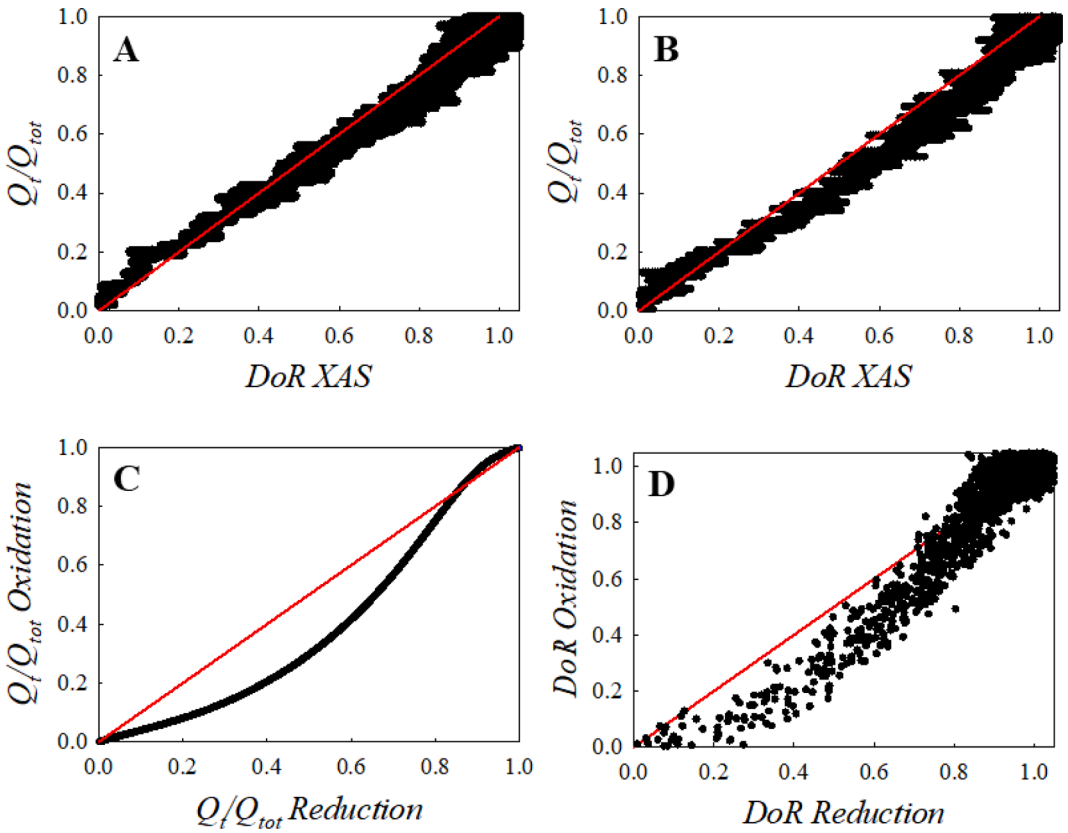

Fig. 4. Results obtained for the Ir(IV) → Ir(III) and Ir(III) → Ir(IV) transitions, for the potential steps 1.05 → 0.2 V and 0.2 → 1.05 V, respectively, in 0.5 M aqueous H_2SO_4. A) Q/Q_{tot} *vs. DoR* for the reduction process; B) Q/Q_{tot} *vs DoR* for the oxidation process; C) Q/Q_{tot} oxidation *vs* Q/Q_{tot} reduction; D) *DoR* oxidation *vs. DoR* reduction.

Therefore, the χ^2 of the fit of the experimental data $y_{exp,\,i}$ to the model was:

$$\sum_i \left\{ y_{exp,i} - \frac{I}{\left(1 - \left[\frac{(x_i - x_0)}{b}\right]^2\right)} - g\left[\frac{1}{2} + \frac{1}{\pi}\arctan\left(\frac{x_i - x_1}{h}\right)\right] \right\}^2 \quad (4)$$

where x_0 is the Lorentzian position, b the Lorentzian width, I the Lorentzian intensity, x_1 the arctangent position, h the arctangent width, g the arctangent intensity, and the index i runs over all energy scan steps of a single spectrum [52]. Reliable starting values of the parameters were found using, on some selected spectra of a sequence, a random Montecarlo search with 3×10^6 steps and checking the consistency of the results along the whole sequence. The parameter values for each spectrum of the sequence were then refined with a variable-metric gradient minimization method, which also determines the parabolic errors.

For each quantity (here indicated by x) showing a sensible variation with time, DoR (ξ) can be calculated from the set of values along the whole sequence according to:

$$\xi = \frac{[x - x_i]}{[x_f - x_i]} \quad (5)$$

where x is the parameter value at current time t, x_i is the value at the initial time t_i, and x_f is the value at the final time t_f. The parameters most suitable for determining a degree of reaction are the Lorentzian position (x_0 in Eq. (3)) and the Lorentzian width (b in Eq. (4)).

The overall procedure for extracting a DoR from the features of an XAS spectrum was selected particularly for its simplicity and ease of implementation on sequences of a large number (thousands) of spectra. Before its routine application to the whole set of experimental data, however, its reliability was assessed by the excellent agreement with the DoR obtained on random sets of XAS spectra using the more conventional approach based on the best fit of a linear combination of suitably selected initial and final spectra.

The third step of the analysis stage (estimation of a kinetic law and of its underlying coefficients) is described in the next section.

3. Results and discussion

The choice of potential steps to be applied was made according to previous works [1] and on the basis of the cyclic voltammetry (CV) runs recorded in aqueous sulfuric acid on the same electrodes used for XAS experiments.

Fig. 2 clearly shows the well-known solid-state redox transition characteristics of IrO_x, represented by reaction (3). A peak couple at about 0.8-0.9 V has been attributed by fixed energy X-ray absorption voltammetries (FEXRAV) [1,53] to the Ir(III)/Ir(IV) reversible transition. In the present case, because of the high loading of IrO_x, ohmic drops are not negligible and the anodic and cathodic peaks are quite separated (Fig. 1 dashed line). In the same figure, the full line shows the CV corrected for the *IR* drop, where R/Ω is the resistance of the layer, which is an adjustable parameter for evaluating the capacitive, I_c, and faradaic, I_f, contributions of the total current I recorded during the appropriate chronoamperometric run. In the forward scan, a small, barely visible, shoulder at about 1.3 V corresponds to the transition Ir (IV)/Ir(V), followed, at higher potentials, by the oxidation of water and the evolution of O_2 [1,54,55].

On the basis of the actual behavior of the EIROF layer, the chronoamperometric + EDXAS runs were recorded upon application of the voltage steps: 0.2 – 1.05 / 1.05 – 0.2 V *vs.* RHE, for observing the Ir(III)/Ir(IV) transitions, and 1.05 – 1.5 / 1.5 – 1.05 V *vs.* RHE, for the

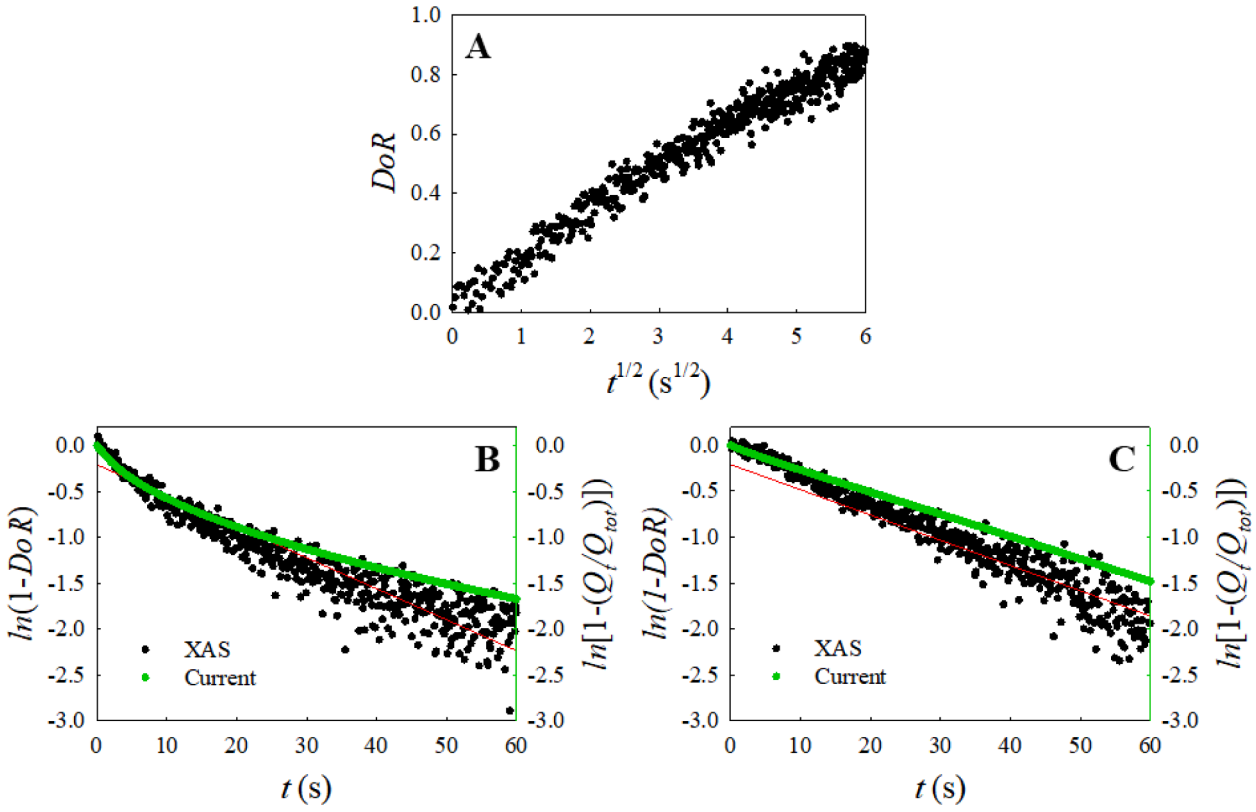

Fig. 5. A: Example of *DoR vs.* $\sqrt{t}$ plot: DoR from XAS for the reduction process. The parabolic trend, which is present in all cases, suggests that the process occurs under diffusion control. B: ln (1-DoR) vs *t* for the reduction process (1.05→0.2 V). C: ln (1-*DoR*) vs *t* for the oxidation process (0.2→1.05 V). The green points refer to Q/Q_{tot}, the black points refer the *DoR* as obtained by XAS, and the red trace shows the asymptotic fitting model described in the text (Eq. (5)).

transitions Ir(IV)/Ir(V). As it will be evident in the following, the latter potential window also includes the H_2O/O_2 reactions.

Fig. 3A exemplifies an Ir-L_{III} XANES spectrum of the IrO_x electrode and Fig. 3B summarizes its time evolution following the potential jump from 1.05 to 0.2 V. Apart from EXAFS oscillations, that are clearly apparent above the noise level, but are of structural origin and will not be taken into account here, the spectrum is mainly composed by a peak (called White Line, WL) due to the transition from 2*p* to empty 5*d* states, and a smooth step that accounts for transitions from 2*p* to continuum states. Both features directly reflect the local electronic structure at the photo-absorber. The main modification evidenced by the time evolution of the XAS is due to changes in the oxidation state. Indeed, the interaction between the nucleus and a 2*p* electron is a screened Coulombic potential and the number of valence electrons determines the screening. The net result is therefore that the energy positions of the spectral features move towards lower values when the oxidation state decreases. This is the well-known chemical shift effect and it is analogous to the chemical shift in photoelectron spectroscopy.

XAS is potentially able to show additional features reflecting finer details of the local electronic structure: crystal field splitting of the 5*d* levels and band formation, for example, both concur in the definition of the exact spectral shape of the WL. A *dispersive* XAS beam line, however, is not fully suited for detecting such fine details and variations thereof, as the energy resolution is not good enough. More important, the energy broadening due to the finite lifetime of the core-hole at the Ir L_{III}-edge amounts to several eV, and therefore hinders subtle spectral features. The main spectral modifications, however, are fully caught as the spectra collected in different conditions display sensible variations. As Fig. 3B shows, after the application of the potential step 1.05 → 0.2 V, the spectra move towards low energy, indicating an overall reduction of Ir from Ir(IV) to Ir(III) and the WL decreases its FWHM, in agreement with previous findings [2,42,56]. The overall time evolution of the two most sensible XAS parameters, position in energy and width of the Lorentzian peak, normalized for their final value in terms of *DoR* are displayed on Fig. 3C and 3D, respectively. These plots also show that the Lorentzian (peak energy) position shows a lower noise and therefore is more reliable. We found this conclusion valid for all XAS experiments and therefore only this parameter will be discussed in the following.

Now, considering the electrochemical data, the current intensity during the potential step directly represents the rate of the faradaic reaction, I_f (but for the first 100-200 ms when the charging of the double layer prevails). Upon integration of the current over time, one obtains the time dependent quantity of charge, *Q*, that, divided by the total quantity of charge, Q_{tot} of the experiment, gives Q/Q_{tot}, the quantity equivalent to the *DoR* expressed by XAS.

Here, two independent measurements are in principle available to quantify the kinetics of the process: (i) the features of XAS spectra that directly give the *DoR* and (ii) the normalized quantity of charge, Q/Q_{tot}, as discussed above.

When each electron exchanged at the electrodes oxidizes or reduces an Ir center, the *DoR* obtained by XAS should be equal to Q/Q_{tot}. This can be experimentally verified using a plot of *DoR* against Q/Q_{tot} (at equal times): if the plot follows the diagonal of the first quadrant, we can reasonably infer that the two techniques monitor the same process. Such plots for the redox process Ir(III)/Ir(IV) monitored in the Ir(IV) →Ir(III) verse, and the reverse one, Ir(III) →Ir(IV), are reported on Fig. 4A and 4B, respectively. We note the impressive agreement found in this case between spectroscopy and electrochemistry. This implies two separate conclusions.

First of all, it directly shows that the Ir(III)/Ir(IV) transitions follow mechanisms free of side reactions or parasitic processes.

As a second point, we understand, despite the surely much higher noise level, that the analysis of XANES features provides an independent determination of the *DoR* of an electrochemical process, that this

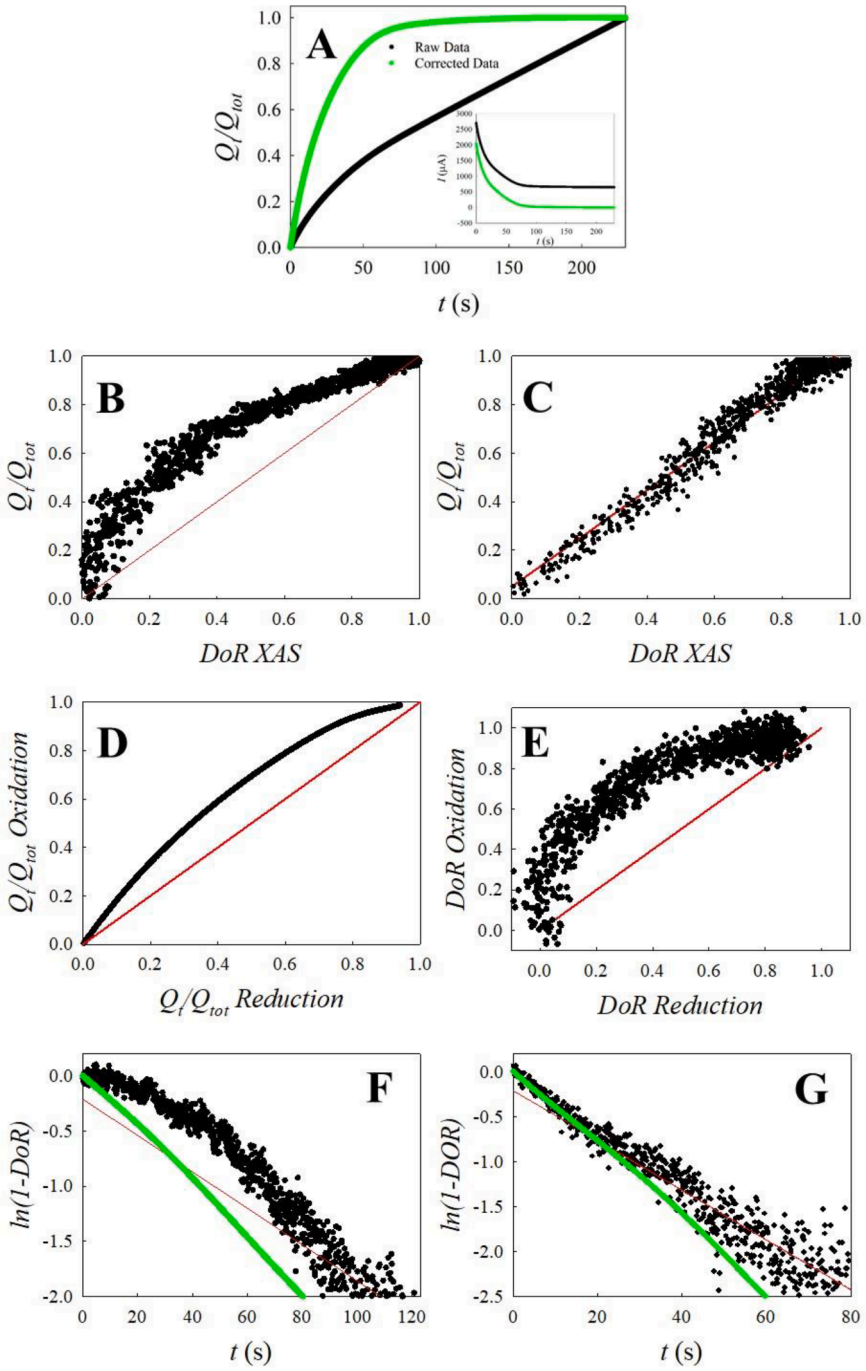

Fig. 6. A. raw current data (inset) and the relevant integrated quantity of charge (Q/Q_{tot}) before (black line) and after (green line) the subtraction of the current due to the OER for the oxidation step. Comparison between Q/Q_{tot} and *DoR XAS* obtained for the potential step 1.5 → 1.05 V are shown in Part B and F and, for the potential step 1.05 → 1.5 V, in parts C and G. Parts B and C shows the DoR obtained by XAS vs. the DoR obtained by the integral of the current (Q/Q_{tot}). Parts D and E show the DoR of oxidation *vs.* the DoR of reduction (obtained from the integral of the current and from XAS, respectively). Parts F and G compare the experimental DoR with fits obtained by means of the model described in Eq. (3). Green points: DoR from the integral of the current; black points: DoR from XAS; red trace: diffusional model.

determination is reliable, and is a potentially powerful tool for clarifying the underlying mechanism of the process.

Going now into deeper detail, we note that, when a reduction process follows the same mechanisms as its corresponding oxidation, also the correlation plot of a *DoR* of oxidation (or Q/Q_{tot}) *vs.* its corresponding *DoR* (Q/Q_{tot}) of reduction should give a straight line with unit slope. These kinds of plots are shown in Fig. 4C and 4D, for the same Ir(III)/Ir(IV) redox process. Both plots show that the reduction is notably faster than oxidation, in particular at the beginning, *i.e.* for $DoR < 0.6$. This can be explained on the basis of the much higher electric resistance of the layer when the majority of Ir sites are in the reduced Ir(III) state of charge [2,57]. At increasing oxidized form, the resistance decreases and the two process finally (DoR > 0.8) exhibit the same rate.

Electron kinetics and charge transfer reactions at porous electrodes have been receiving increasing attention [58–61] because of their wide applications in energy conversion devices (electrochemical generators, capacitors and electrolyzers) and in chemically modified sensors [62]. The most common picture considers an electroactive component supported on a low-activity carbon matrix, so that comparison can be made in presence and in absence of the active material [63].

In case of the pseudo-capacitive reaction (3) it is a common understanding that the rate-determining step of the redox processes involving the IrO_x centers is the diffusion of H^+ ions in the layer. This understanding is supported by the plot(s) of the DoR of the Ir(IV) → Ir(III) process *vs.* time (Fig. 3C, D): these show an immediately detectable parabolic behaviour that is typical of diffusion driven processes, and is better seen in Fig 5A, where the DoR is plotted vs. $\sqrt{t}$. Slight deviations from the linear behaviour are detected after the first 10 s. These

deviations are small and are probably because, as the reaction progresses, the number of active sites decreases, which means that the less accessible sites are those that persists, and therefore different diffusion path may limit the overall kinetics.

Thus, the time evolution of the *DoR* data can be used for extracting the proton diffusion coefficient by adopting an appropriate model. To that purpose, we heuristically try a 1D model based on a porous electrode layer of thickness *L* enclosed between a compact metal body and a large volume of liquid electrolyte. This acts as an unlimited source of the H^+ diffusing species at constant concentration, which is different from the value corresponding to electrochemical equilibrium at the new electrode potential. The result of this approach ([64,35], see also **the appendix** for details) gives:

$$\frac{n(t)}{n_s} = 1 - \frac{8}{\pi^2}\sum_{i=0}^{\infty}\frac{1}{(2i+1)^2}e^{\frac{-(2i+1)^2\pi^2 Dt}{L^2}} \quad (6)$$

Here $n(t)$ is the total amount of the diffusing species that has entered the electrode layer up to time *t*, n_s is the corresponding asymptotic quantity (at long enough times), and *D* is an effective diffusion coefficient. Basically, *D* is the diffusion coefficient in the liquid electrolyte modified by factors accounting for the porosity of the electrolyte layer and occurrence of the electrode reaction along the whole porous layer ([64,35] and SI). Assuming that diffusion in the layer is the rds, the left hand-side of Eq. (6) is a *DoR* and is suitable for direct comparison with experimental data. To this purpose, the asymptotic expression:

$$\xi = \frac{n(t)}{n_s} = 1 - \frac{8}{\pi^2}e^{-\frac{\pi^2 Dt}{L^2}} \quad (7)$$

is sometimes used for its simplicity, as it gives a linear plot of $ln[1-\xi]$ *vs. t* (see appendix, Fig 8). More precisely, on a $ln[1-\xi]$ *vs. t* plot the kinetic model describes an almost linear trend at "high enough" times. The asymptotic straight line wrongly extrapolates to $ln(1-8/\pi^2) \approx$ -0.21 at $t = 0$, while the full model correctly bends up at "low" times to $ln[1-\xi] = 0$ at $t = 0$.

We can now test the model described in Eq. (6) against the experimental data. Starting from the reduction reaction (1.05 → 0.2 V, Fig. 5B), it is well apparent that the XAS data are well interpreted for $t >$ 5 s *ca.* by the linear trend of Eq (7), and in the whole time range by Eq (6), which accounts for the initial curvature. Thus, it can be safely concluded that the Ir(IV) → Ir(III) reduction is controlled by diffusion in the whole time range, in particular up to the virtual end of the reaction. The diffusion coefficient, obtained by the fit of the linear part of the plot in Fig. 5B is 4.3×10^{-6} $cm^2 \bullet s^{-1}$.

For the Ir(III) → Ir(IV) oxidation (0.2 → 1.05 V), *DoR* (Fig. 5C) shows many distinctive features of the diffusional model: there is a well apparent linear trend of $ln[1-\xi]$ vs. *t* after about 15 s, the linear trend correctly extrapolates to $\ln(8/\pi^2)$ for $t = 0$, and the $ln[1-\xi]$ quantity correctly goes to zero at $t = 0$ as required by the full model (Eq. (6)). Initially, however, the *DoR* data distinctively stay above (lower *DoR*) the trace of the full model and appear as remarkably smaller than their counterpart in the reduction run.

The second case discussed in this work, Fig. 6 A-G, refers to chronoamperometric programs corresponding to the potential steps 1.5 V → 1.05 V and 1.05 V → 1.5 V, where oxygen evolution indeed occurs.

In the latter case, the *DoR* cannot be directly compared with the time integral of the current. The latter quantity, indeed, does not go to zero at long enough times, as expected from the occurrence an uninterrupted oxygen evolution. In the oxidation run, therefore, a constant current value has been determined from the current signal at "long" times, and the value has been preliminarily subtracted to the raw current data. The trends for the current and for Q/Q_{tot} before and after subtraction are shown in Fig. 6A

For both the potential step-down and the potential step-up runs, the correlation plots of *DoR vs.* Q_t/Q_{tot} (Fig. 6B and C, respectively) clearly show that spectroscopy and electrochemistry determine different processes. According to the first plot (Fig. 6B), the processes monitored by the current are globally faster than Ir reduction (monitored by XAS), an indication that another process occurs in parallel with Ir reduction and that will be further discussed later. On the other hand, Fig. 6C seemingly indicates that the variation in Ir oxidation state occurs at a rate comparable to the exchange of electrons (after subtraction of the contribution of oxygen evolution, that contributed with a constant current for the length of this experiment). Some difference can be however remarked and is better discussed using the following plots. Fig. 6D and E show that reduction and oxidation follow different rate laws, and reduction appears regularly slower than oxidation. Finally, Fig. 6F and G can provide some mechanistic information. Let us start with Fig. 6G. Here *DoR* shows all features required by the previously presented diffusional model: linear trend at high times, extrapolation of the linear trend to $\ln(8/\pi^2)$ for $t = 0$, upwards curvature of the trend of the initial data. The *D* value is then *ca.* 5.2×10^{-6} $cm^2 \bullet s^{-1}$. For the same process, Q_t/Q_{tot} initially agrees with *DoR*, then is regularly larger, and follow a roughly linear trend that is not consistent with the features of the diffusional model. In this case a tentative explanation evolves the oxygen evolution related to the formation of Ir(V) clusters. If the explanation is correct, the formation of proximal Ir(V)-Ir(V) couples occurs after *ca.* 20 s [55]. At this moment, XAS and electrochemical signal separate because the OER proceeds with a slower oxidation of Ir, that progressively enters a catalytic cycle where it is oxidation state likely sweeps between two extremes values (likely (III) and (V)[2]). This proofs that the OER is anticipated by the oxidation of Ir, a process that is controlled by the diffusion of charged species (H^+) towards the solution.

Going now to the reduction run (Fig. 6F), we immediately see that Ir reduction accounts for only part of the charge exchanged and that *DoR* and Q_t/Q_{tot} do not show the features required by the diffusional model. A tentative fit, that only considers the final moments of the reduction, leads to a value of *D* of about 3.1×10^6 cm^2 s^{-1}. As anticipated, this is an indication that another process occurs in parallel with Ir reduction. This additional process might be a residual contribution of the OER that occurs at the initial stages of the step, when only part of the material is reduced.

Table 1
Diffusion coefficients estimated with the model described by Eq. (7) for all the reduction/oxidation processes investigated.

H^+ Diffusion Coefficients ($cm^2 \bullet s^{-1}$)		
Couple	Reduction	Oxidation
Ir(III)/Ir(IV)	4.3×10^{-6}	3.8×10^{-6}
Ir(IV)/Ir(V)	3.1×10^{-6}	5.2×10^{-6}

Table 1 summarizes the diffusion coefficients estimated by means of Eq. (7) for all the potential steps applied leading to Ir(III)/Ir(IV) and Ir (IV)/Ir(V) transitions. All the values obtained are of the order of 10^{-6} $cm^2 \bullet s^{-1}$.

We could not find several comparable data in the literature but for the work by Pauportè on sputtered iridium oxide films (SPIROFs) [65] where *D* was determined by electrochemical impedance spectroscopy, EIS, and the reported data range from 2×10^{-8} to 1.1×10^{-7} $cm^2 \bullet s^{-1}$ from 0.4 to 1 V (SCE) in 1 M H_2SO_4. The same approach was adopted here to further validate the operando EDXAS approach and confirm the relevant results.

Here we adopted the same equivalent circuit adopted for sputtered iridium oxide films [65], that is a simple Randles circuit plus a resistance accounting for the solution impedance (Fig. 7 inset). All EIS spectra have been fitted with the ZView software, adopting a Warburg open to describing a one-dimensional diffusion with a blocked boundary:

$$Z = R\frac{\coth[(iT\omega)^p]}{(iT\omega)^p} \quad (8)$$

Where *Z* is the impedance, ω the frequency, *i* the imaginary unit and *R* the resistance associated to the Warburg element and *T* is the

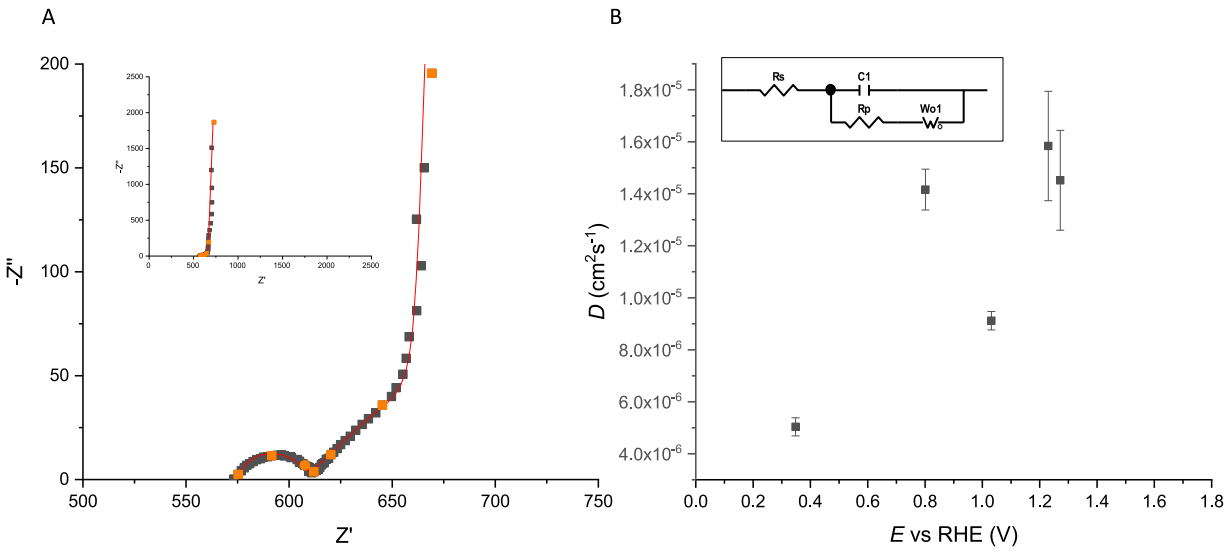

Fig. 7. A. Magnification of the Nyquist plot for the EIS spectra recorded at 1.03 V. The full spectrum is reported in the inset. Black squares are the experimental values, the orange line represents the fitting line. **B.** Diffusion coefficient, D, as a function of the applied potential, extracted from the Warburg element in the equivalent circuit reported in the inset, where R_s is the solution resistance, C_1 the double layer capacitance (here a constant phase element was used instead of a capacitance), R_p the faradaic resistance and W_{O1} the Warburg open element.

reciprocal the diffusion time constant, K_n.[66]

The good quality of the fit is proven by Fig. 7A, together with the typical shape of the Nyquist plot for a porous media that includes a blocked boundary finite-length Warburg impedance.

The raw data fit allow the determination of T, that is related to the diffusion coefficient, D (shown in Fig. 7B) by the following equation [67]:

$$D = \frac{L^2}{T} \tag{9}$$

Here we assume that the length of the diffusion thickness, L, coincides with the thickness of the IrO_2 layer and that, working in a concentrated acid solution, the charge transport within the film is dominated by H^+ ions.

Although leading to higher values for D, EIS confirms that the diffusion coefficient of proton in EIROF is significantly higher than on other materials, *e.g.* r.f. sputtered IrO_2, and even higher than for films obtained by magnetron sputtering ($D = 4.5\times10^{-13}$ [68] or between 10^{-11} and 10^{-10} $cm^2 \bullet s^{-1}$[69]). We attribute the higher values obtained in the present work to a significantly higher hydration degree of EIROF compared to SPIROF, leaving wider pathways for H^+ transport.

4. Conclusions

In the present work we studied the kinetics associated to highly hydrated IrO_x films in different chronoamperometric conditions, by means of energy dispersive-XAS spectroscopy, leading to the first direct quantification of the diffusion coefficient of protons into an iridium oxide electrode. Thanks to the combination of spectroscopic and electrochemical measurements, we managed to obtain two independent sets of data. This is needed to fully assess the mechanistic insights, since it allows to identify any parasitic effect or side reaction. Experiments were carried out in acidic medium and the final time resolution of XAS spectra acquired is 0.116 s. For each sequence, all spectra were fitted automatically by a linear combination of a Lorentzian and an Arctangent employing Minuit software. Reliable *DoRs* were obtained from Lorentzian positions: the parabolic trends *vs.* time clearly accounts for a diffusion driven control, and the diffusion coefficient, which were obtained by extrapolation, are of the order of 10^{-6} $cm^2 \bullet s^{-1}$. Two are the potential windows investigated in this experiment: (*i*) 0.2 —1.05 V, in which the oxidation state of Ir ranges from Ir(III) and Ir(IV) and (*ii*) 1.05—1.5 V, in which Ir reaches the Ir(V) oxidation state and oxygen evolution begins.

(i) In the first case, the system behaves as a pseudocapacitance with an H^+ diffusion-controlled kinetics. Spectroscopy and electrochemistry agree on the kinetic trends. The reduction process is clearly faster than the oxidation one. Furthermore, both the reduction and oxidation reactions can be well interpreted by the diffusion model of a finite layer with an infinite source of protons described in Eqs. (5) and (6).

(ii) For the potential window 1.05—1.5 V, spectroscopy and electrochemistry do not agree, particularly for the potential step down. Quite interestingly, the model described in Eq. (5) is well interpreted when the potential step is 1.05 V → 1.5 V, after the current deriving from water oxidation was subtracted. On the contrary, the model cannot be applied to the results obtained for the step 1.5 V → 1.05 V. A hypothesis to this can be the occurrence of an electrochemical process that does not change the oxidation state of Ir. For example, a contribution from the oxygen evolution reaction that persists in the initial part of the step and that could not be easily ruled out from the chronoamperometry data.

CRediT authorship contribution statement

Elisabetta Achilli: Writing – original draft, Writing – review & editing, Investigation, Data curation, Visualization, Formal analysis. **Simone Minelli:** Investigation, Resources, Visualization, Formal analysis. **Irene Casale:** Investigation, Resources. **Xiufang He:** Investigation, Resources, Visualization. **Giovanni Agostini:** Investigation, Resources. **Giorgio Spinolo:** Formal analysis, Software, Data curation. **Paolo Ghigna:** Conceptualization, Funding acquisition, Writing – original draft, Supervision, Visualization, Project administration. **Alessandro Minguzzi:** Conceptualization, Funding acquisition, Writing – original draft, Writing – review & editing, Supervision, Methodology, Visualization, Project administration, Investigation, Resources. **Alberto Vertova:** Project administration, Resources, Validation, Conceptualization, Supervision.

Declaration of Competing Interest

The authors declare the following financial interests/personal relationships which may be considered as potential competing interests:

Alberto Vertova reports financial support was provided by

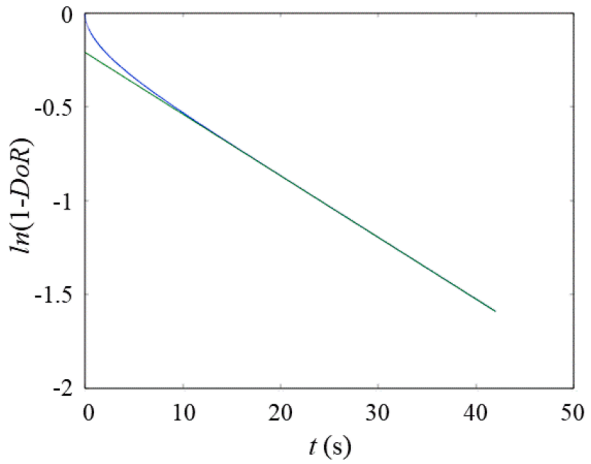

Fig. 8. Simulation providing the graphical analysis of Eq. (10), where ξ is renamed as a degree of reaction (DoR).

Government of Italy Ministry of Education University and Research.

Data availability

Data will be made available on request.

Acknowledgments

The authors gratefully acknowledge the European Synchrotron Radiation Facility for provision of beam time (experiment CH-4090). Miur – PRIN 2017, Prot. 2017YH9MRK: "Novel Multilayered and Micro-Machined Electrode Nano-Architectures for Electrocatalytic Applications (Fuel Cells and Electrolyzers)'' and Università degli Studi di Milano, Piano di Sostegno alla Ricerca, Linea 2A and Linea 6 "One Health Action Hub: University Task Force for the resilience of territorial ecosystems" are also acknowledged for financial support. A.M. acknowledges project PNRR - Partenariati estesi - NEST - Network 4 Energy Sustainable Transition" - PE0000021 for partial funding.

Appendix diffusion model for transient experiments (ED-XAS / chronoamperometries)

Here we describe the diffusion model adopted for the interpretation of EDXAS results.

(1) The texture of the porous EIROF electrode is modeled as an array of electronically conductive Ir oxide nano-rods embedded in a liquid electrolyte matrix or, in an equivalent way, as an array of electrolyte-filled cylindrical pores of an Ir oxide matrix.
(2) We assume that the bulk liquid electrolyte solution ahead of the electrode assembly is well stirred and that concentration and overall amount of electrolyte are so large that we can neglect any change of its concentration in time or space in this external solution.
(3) We now consider the diffusion problem in a homogeneous layer with thickness L with a uniform and constant diffusion coefficient D, where the concentration of the diffusing species is constrained at the equilibrium value C_{eq} at $x = 0$ ($t \geq 0$) and at a (different) initial value C_0 in the whole range $0 < x < L$ (at $t = 0$) and also for all times at $x = L$. The solution of the problem (as reported by Crank [64] Eq. (4).23 pag. 50) is:

$$\frac{q(t)}{q_s} = 1 - \frac{8}{\pi^2}\sum_{n=0}^{\infty}\frac{1}{(2n+1)^2}e^{\frac{-(2n+1)^2\pi^2 Dt}{L^2}}, \tag{10}$$

where $q(t)$ is the total amount that has entered the layer at time t, while q_s is the corresponding quantity at long times. To tailor this solution to our problem, we must preliminarily account for texture of the porous electrode layer and for the electrochemical reaction. For both problems we again refer to arguments discussed by Crank [64].
(4) The heterogeneous texture with axial symmetry (along the diffusion direction) can be accounted for by an effective-medium approach, which clearly neglects gradients along normal directions, shape effects, and non-uniform sizes, widths, and surface areas of the rods and/or pores. Within this approximate treatment, the previous solution can be modified by simply using a different diffusion coefficient (D'), which is essentially the same D rescaled by the ratio of the overall cross-section of the liquid channels to the whole area of the electrode assembly.
(5) Within the same effective-medium approach, the electrochemical reaction occurring at the whole contact surface between Ir oxide particles and the embedding liquid electrolyte is accounted for as a *homogeneous* chemical reaction occurring along the whole thickness L of the electrode assembly layer.
(6) We refer here to another standard problem in diffusion, where "some of the diffusing substance becomes immobilized as diffusion proceeds: diffusion may take place within the pores of a solid body" [64]. We also assume that "the reaction by which the immobilized reactant is formed proceeds very rapidly compared with the diffusion process": local equilibrium can be assumed to exist between the free (H_3O^+) and immobilized. Ir(III) or Ir(IV) species and the activities or concentrations are proportional to each other. Within these assumptions, the previous solution to the diffusion problem can still be used, after replacing the previous diffusion coefficient (D') with a new parameter including the reaction rate R: $D'' = D' / (R + 1)$.
(7) We note that Eq. (9) already represents a degree of reaction and is suitable to direct comparison with experiments. To this purpose, the asymptotic expression:

$$\xi = \frac{q(t)}{q_s} = 1 - \frac{8}{\pi^2}e^{-\frac{\pi^2 Dt}{L^2}} \tag{11}$$

can be used. By giving a linear relation (Fig. 8) between the experimentally measured quantity $ln[1-\xi]$ vs. t, this simplified (asymptotic) form provides an important way for a graphical control of the agreement of the experimental data to the model, and a fast tool for determining the pertinent diffusion coefficient (D'').

We warn, however, that the asymptotic form holds for "long enough" times and it is indeed possible to detect deviations from the linear trend in

form of an upwards curvature at "small times". The asymptotic straight line extrapolates to $\xi = \ln(8/\pi^2) \approx$ - 0.21 (independent of *D, T* and other experiment-specific variables), while the full expression correctly goes to $\xi = 0$ [= ln (1)] at the initial time.

References

[1] A. Minguzzi, O. Lugaresi, C. Locatelli, S. Rondinini, F. D'Acapito, E. Achilli, P. Ghigna, Fixed energy X-ray absorption voltammetry, Anal. Chem. 85 (2013) 7009–7013, https://doi.org/10.1021/ac401414v.

[2] A. Minguzzi, O. Lugaresi, E. Achilli, C. Locatelli, A. Vertova, P. Ghigna, S. Rondinini, Observing the oxidation state turnover in heterogeneous iridium-based water oxidation catalysts, Chem. Sci. 5 (2014) 3591–3597, https://doi.org/10.1039/C4SC00975D.

[3] A. Minguzzi, A. Naldoni, O. Lugaresi, E. Achilli, F. D'Acapito, F. Malara, C. Locatelli, A. Vertova, S. Rondinini, P. Ghigna, Observation of charge transfer cascades in α-Fe $_2$ O $_3$ /IrO $_x$ photoanodes by operando X-ray absorption spectroscopy, Phys. Chem. Chem. Phys. 19 (2017) 5715–5720, https://doi.org/10.1039/C6CP08053G.

[4] T. Baran, M. Fracchia, A. Vertova, E. Achilli, A. Naldoni, F. Malara, G. Rossi, S. Rondinini, P. Ghigna, A. Minguzzi, F. D'Acapito, Operando and time-resolved X-ray absorption spectroscopy for the study of photoelectrode architectures, Electrochim. Acta 207 (2016) 16–21, https://doi.org/10.1016/j.electacta.2016.04.153.

[5] R.H.G. Mingels, S. Kalsi, Y. Cheong, H. Morgan, Iridium and Ruthenium oxide miniature pH sensors: long-term performance, Sens. Actuators B Chem (2019) 297, https://doi.org/10.1016/j.snb.2019.126779.

[6] S.J. Kwon, F.R.F. Fan, A.J. Bard, Observing iridium oxide (IrOx) single nanoparticle collisions at ultramicroelectrodes, J. Am. Chem. Soc. 132 (2010) 13165–13167, https://doi.org/10.1021/ja106054c.

[7] A. Minguzzi, F.R.F. Fan, A. Vertova, S. Rondinini, A.J. Bard, Dynamic potential–pH diagrams application to electrocatalysts for water oxidation, Chem. Sci. 3 (2012) 217, https://doi.org/10.1039/c1sc00516b.

[8] C.C.L. McCrory, S. Jung, I.M. Ferrer, S.M. Chatman, J.C. Peters, T.F. Jaramillo, Benchmarking hydrogen evolving reaction and oxygen evolving reaction electrocatalysts for solar water splitting devices, J. Am. Chem. Soc. 137 (2015) 4347–4357, https://doi.org/10.1021/ja510442p.

[9] C.C.L. McCrory, S. Jung, J.C. Peters, T.F. Jaramillo, Benchmarking heterogeneous electrocatalysts for the oxygen evolution reaction, J. Am. Chem. Soc. 135 (2013) 16977–16987, https://doi.org/10.1021/ja407115p.

[10] a. Vertova, L. Borgese, G. Cappelletti, C. Locatelli, a. Minguzzi, C. Pezzoni, S. Rondinini, New electrocatalytic materials based on mixed metal oxides: Electrochemical quartz crystal microbalance characterization, J. Appl. Electrochem. 38 (2008) 973–978, https://doi.org/10.1007/s10800-008-9510-x.

[11] E. Guerrini, H. Chen, S. Trasatti, Oxygen evolution on aged IrO x /Ti electrodes in alkaline solutions, J. Solid State Electrochem. 11 (2007) 939–945, https://doi.org/10.1007/s10008-006-0238-4.

[12] C. Locatelli, A. Minguzzi, A. Vertova, S. Rondinini, IrO2-SnO2 mixtures as electrocatalysts for the oxygen reduction reaction in alkaline media, J. Appl. Electrochem. (2013) 43, https://doi.org/10.1007/s10800-012-0520-3.

[13] M. Carmo, D.L. Fritz, J. Mergel, D. Stolten, A comprehensive review on PEM water electrolysis, Int. J. Hydrog. Energy. 38 (2013) 4901–4934, https://doi.org/10.1016/j.ijhydene.2013.01.151.

[14] A. Minguzzi, C. Locatelli, G. Cappelletti, C.L. Bianchi, A. Vertova, S. Ardizzone, S. Rondinini, Designing materials by means of the cavity-microelectrode: The introduction of the quantitative rapid screening toward a highly efficient catalyst for water oxidation, J. Mater. Chem. (2012) 22, https://doi.org/10.1039/c2jm15750k.

[15] S. Ardizzone, C.L. Bianchi, G. Cappelletti, M. Ionita, A. Minguzzi, S. Rondinini, A. Vertova, Composite ternary SnO<inf>2</inf>-IrO<inf>2</inf>-Ta<inf>2</inf>O<inf>5</inf>oxide electrocatalysts, J. Electroanal. Chem. (2006) 589, https://doi.org/10.1016/j.jelechem.2006.02.004.

[16] P. Pedeferri, Cathodic protection, Corrosion and Corrosion Protection Handbook 10 (2017) 33–46, https://doi.org/10.1201/9781315140384.

[17] W. Zhang, E. Ghali, G. Houlachi, Review of oxide coated catalytic titanium anodes performance for metal electrowinning, Hydrometallurgy 169 (2017) 456–467, https://doi.org/10.1016/j.hydromet.2017.02.014.

[18] P. Steegstra, E. Ahlberg, Involvement of nanoparticles in the electrodeposition of hydrous iridium oxide films, Electrochim. Acta 68 (2012) 206–213, https://doi.org/10.1016/j.electacta.2012.02.058.

[19] K. Yamanaka, Anodically electrodeposited iridium oxide films (AEIROF) from alkaline solutions for electrochromic display devices, Jpn. J. Appl. Phys. 28 (1989) 632–637, https://doi.org/10.1143/JJAP.28.632.

[20] M.a. Petit, V. Plichon, Anodic electrodeposition of iridium oxide films, J. Electroanal. Chem. 444 (1998) 247–252, https://doi.org/10.1016/S0022-0728(97)00570-6.

[21] S. Geiger, O. Kasian, M. Ledendecker, E. Pizzutilo, A.M. Mingers, W.T. Fu, O. Diaz-Morales, Z. Li, T. Oellers, L. Fruchter, A. Ludwig, K.J.J. Mayrhofer, M.T.M. Koper, S. Cherevko, The stability number as a metric for electrocatalyst stability benchmarking, Nat. Catal. 1 (2018) 508–515, https://doi.org/10.1038/s41929-018-0085-6.

[22] N. Danilovic, R. Subbaraman, K.C. Chang, S.H. Chang, Y.J. Kang, J. Snyder, A. P. Paulikas, D. Strmcnik, Y.T. Kim, D. Myers, V.R. Stamenkovic, N.M. Markovic, Activity-stability trends for the oxygen evolution reaction on monometallic oxides in acidic environments, J. Phys. Chem. Lett. 5 (2014) 2474–2478, https://doi.org/10.1021/jz501061n.

[23] S. Cherevko, S. Geiger, O. Kasian, A. Mingers, K.J.J. Mayrhofer, Oxygen evolution activity and stability of iridium in acidic media. Part 2. - Electrochemically grown hydrous iridium oxide, J. Electroanal. Chem. 774 (2016) 102–110, https://doi.org/10.1016/j.jelechem.2016.05.015.

[24] P.G. Pickup, V.I. Birss, Chemical analysis of the ionic content of hydrous iridium oxide films, J. Electroanal. Chem. 240 (1988) 171–183, https://doi.org/10.1016/0022-0728(88)80321-8.

[25] S. Roy, D. Bagchi, L. Dheer, S.C. Sarma, V. Rajaji, C. Narayana, U.V. Waghmare, S. C. Peter, Mechanistic insights into the promotional effect of Ni substitution in non-noble metal carbides for highly enhanced water splitting, Appl. Catal. B Environ. (2021) 298, https://doi.org/10.1016/j.apcatb.2021.120560.

[26] G. Cappelletti, E. Pargoletti, A. Minguzzi, A. Vertova, S. Rondinini, Effect of pure and AG-doped Mno<inf>2</inf>nanoparticles on the Li-air cathode behaviour, in: Proceedings of the World Congress on New Technologies, 2015.

[27] C.P. De Pauli, S. Trasatti, Composite materials for electrocatalysis of O2 evolution : IrO2+SnO2 in acid solution, 539 (2002) 145–151.

[28] S. Trasatti, Electrocatalysis in the anodic evolution oxygen and chlorine, 29 (1984) 1503–1512.

[29] L.D. Burke, O.J. Murphy, Cyclic voltammetry as a technique for determining the surface area of RuO2 electrodes, J. Electroanal. Chem. 96 (1979) 19–27, https://doi.org/10.1016/S0022-0728(79)80299-5.

[30] S. Ardizzone, G. Fregonara, S. Trasatti, Inner" and "outer" active surface of RuO2 electrodes, Electrochim. Acta 35 (1990) 263–267, https://doi.org/10.1016/0013-4686(90)85068-X.

[31] T. Reier, Z. Pawolek, S. Cherevko, M. Bruns, T. Jones, D. Teschner, S. Selve, A. Bergmann, H.N. Nong, R. Schlögl, K.J.J. Mayrhofer, P. Strasser, Molecular insight in structure and activity of highly efficient, low-Ir Ir-Ni oxide catalysts for electrochemical water splitting (OER), J. Am. Chem. Soc. 137 (2015) 13031–13040, https://doi.org/10.1021/jacs.5b07788.

[32] M. Ekimova, C. Kleine, J. Ludwig, M. Ochmann, T.E.G. Agrenius, E. Kozari, D. Pines, E. Pines, N. Huse, P. Wernet, M. Odelius, E.T.J. Nibbering, From Local Covalent Bonding to Extended Electric Field Interactions in Proton Hydration, Angew. Chem. Int. Ed 61 (2022), https://doi.org/10.1002/anie.202211066.

[33] S. Trasatti, Electrodes of Conductive Metallic Oxides, Elsevier Scientific Publishing Company, Amsterdam, 1980.

[34] J. Timoshenko, B. Roldan Cuenya, *In situ*/operando electrocatalyst characterization by X-ray absorption spectroscopy, Chem. Rev. 121 (2021) 882–961, https://doi.org/10.1021/acs.chemrev.0c00396.

[35] P. Ghigna, S. Rondinini, M. Fracchia, A. Vertova, A. Minguzzi, Time-resolved X-ray absorption spectroscopy in (Photo)electrochemistry, Surfaces 1 (2018) 138–150, https://doi.org/10.3390/surfaces1010011.

[36] A. Minguzzi, P. Ghigna, A.J. Bard, C.G. Zoski, X-ray absorption spectroscopy in electrochemistry from fundamentals to fixed energy X-ray absorption voltammetry, in: Electroanalytical Chemistry, A Series of Advances, 27, CRC Press - Taylor and Francis Group, USA, 2017, pp. 119–181, https://doi.org/10.1201/9781315270302.

[37] R. O'Malley, A. Vollmer, J. Lee, I. Harvey, J. Headspith, S. Diaz-Moreno, T. Rayment, Time-resolved studies of diffusion via energy dispersive X-ray absorption spectroscopy, Electrochem. Commun. 5 (2003) 1–5. http://www.sciencedirect.com/science/article/pii/S1388248102005167.

[38] L. Plais, C. Lancelot, C. Lamonier, E. Payen, V. Briois, First *in situ* temperature quantification of CoMoS species upon gas sulfidation enabled by new insight on cobalt sulfide formation, Catal. Today 377 (2021) 114–126, https://doi.org/10.1016/j.cattod.2020.06.065.

[39] C. Prestipino, O. Mathon, R. Hino, A. Beteva, S. Pascarelli, Quick-EXAFS implementation on the general purpose EXAFS beamline at ESRF, J. Synchrotron Radiat. 18 (2011) 176–182, https://doi.org/10.1107/S0909049510046546.

[40] A. Rose, O. South, I. Harvey, S. Diaz-Moreno, J.R. Owen, A.E. Russell, *In situ* time resolved studies of hydride and deuteride formation in Pd/C electrodes via energy dispersive X-ray absorption spectroscopy, Phys. Chem. Chem. Phys. 7 (2005) 366–372, https://doi.org/10.1039/b412066c.

[41] S.C. Lin, C.C. Chang, S.Y. Chiu, H.T. Pai, T.Y. Liao, C.S. Hsu, W.H. Chiang, M. K. Tsai, H.M. Chen, Operando time-resolved X-ray absorption spectroscopy reveals the chemical nature enabling highly selective CO2 reduction, Nat. Commun. 11 (2020) 3525, https://doi.org/10.1038/s41467-020-17231-3.

[42] S. Rondinini, A. Minguzzi, E. Achilli, C. Locatelli, G. Agostini, G. Spinolo, A. Vertova, P. Ghigna, The dynamics of pseudocapacitive phenomena studied by Energy Dispersive XAS on hydrous iridium oxide electrodes in alkaline media, Electrochim. Acta 212 (2016) 247–253, https://doi.org/10.1016/j.electacta.2016.06.149.

[43] A. Minguzzi, L. Montagna, A. Falqui, A. Vertova, S. Rondinini, P. Ghigna, Dynamics of oxide growth on Pt nanoparticles electrodes in the presence of competing halides by operando energy dispersive X-Ray absorption spectroscopy, Electrochim. Acta 270 (2018) 378–386, https://doi.org/10.1016/j.electacta.2018.03.092.

[44] E. Achilli, A. Minguzzi, O. Lugaresi, C. Locatelli, S. Rondinini, G. Spinolo, P. Ghigna, *In situ* dispersive EXAFS in electrocatalysis : the investigation of the local structure of IrO ? in chronoamperometric conditions as a case study, J. Spectrosc. 2014 (2014). Article ID 480102.

[45] A. Battistel, F.La Mantia, On the physical definition of dynamic impedance: How to design an optimal strategy for data extraction, Electrochim. Acta 304 (2019) 513–520, https://doi.org/10.1016/j.electacta.2019.03.033.
[46] A.T. Tran, F. Huet, K. Ngo, P. Rousseau, Artefacts in electrochemical impedance measurement in electrolytic solutions due to the reference electrode, Electrochim. Acta 56 (2011) 8034–8039, https://doi.org/10.1016/j.electacta.2010.12.088.
[47] S. Pascarelli, O. Mathon, M. Muñoz, T. Mairs, J. Susini, Energy-dispersive absorption spectroscopy for hard-X-ray micro-XAS applications, J. Synchrotron Radiat. 13 (2006) 351–358, https://doi.org/10.1107/S0909049506026938.
[48] S. Pascarelli, O. Mathon, Advances in high brilliance energy dispersive X-ray absorption spectroscopy, Phys. Chem. Chem. Phys. 12 (2010) 5535–5546, https://doi.org/10.1039/b926434e.
[49] J.-C. Labiche, O. Mathon, S. Pascarelli, M.A. Newton, G.G. Ferre, C. Curfs, G.B. M. Vaughan, A. Homs, D.F. Carreiras, The fast readout low noise camera as a versatile x-ray detector for time resolved dispersive extended x-ray absorption fine structure and diffraction studies of dynamic problems in materials science, chemistry, and catalysis, Rev. Sci. Instrum. 78 (2007) 91301, https://doi.org/10.1063/1.2783112.
[50] S.J.A. Figueroa, C. Prestipino, PrestoPronto: a code devoted to handling large data sets, J. Phys. Conf. Ser. 712 (2016), 012012, https://doi.org/10.1088/1742-6596/712/1/012012.
[51] MINUIT – function minimization and error analysis, CERN Program Library entry D506., (2023).
[52] P. Ghigna, G. Spinolo, M. Scavini, U.A. Tamburini, A.V. Chadwick, The atomic and electronic structure of cerium substitutional defects in Nd2−xCexCuO4+δ An XAS study, Phys. C Supercond. 253 (1995) 147–155, https://doi.org/10.1016/0921-4534(95)00497-1.
[53] S. Rondinini, O. Lugaresi, E. Achilli, C. Locatelli, A. Vertova, P. Ghigna, A. Minguzzi, C. Comninellis, Fixed energy X-ray absorption voltammetry and extended X-ray absorption fine structure of Ag nanoparticle electrodes, J. Electroanal. Chem. 766 (2016) 71–77, https://doi.org/10.1016/j.jelechem.2016.01.039.
[54] L. Ouattara, S. Fierro, O. Frey, M. Koudelka, C. Comninellis, Electrochemical comparison of IrO2 prepared by anodic oxidation of pure iridium and IrO2 prepared by thermal decomposition of H 2IrCl6 precursor solution, J. Appl. Electrochem. 39 (2009) 1361–1367, https://doi.org/10.1007/s10800-009-9809-2.
[55] P. Steegstra, M. Busch, I. Panas, E. Ahlberg, Revisiting the redox properties of hydrous iridium oxide films in the context of oxygen evolution, J. Phys. Chem. C 117 (2013) 20975–20981.
[56] A. Minguzzi, C. Locatelli, O. Lugaresi, E. Achilli, G. Cappelletti, M. Scavini, M. Coduri, P. Masala, B. Sacchi, A. Vertova, P. Ghigna, S. Rondinini, Easy accommodation of different oxidation states in iridium oxide nanoparticles with different hydration degree as water oxidation electrocatalysts, ACS Catal. 5 (2015) 5104–5115, https://doi.org/10.1021/acscatal.5b01281.
[57] I.A. Lervik, M. Tsypkin, L.E. Owe, S. Sunde, Electronic structure vs. electrocatalytic activity of iridium oxide, J. Electroanal. Chem. 645 (2010) 135–142, https://doi.org/10.1016/j.jelechem.2010.04.024.
[58] J. Masa, C. Batchelor-McAuley, W. Schuhmann, R.G. Compton, Koutecky-Levich analysis applied to nanoparticle modified rotating disk electrodes: Electrocatalysis or misinterpretation, Nano Res. 7 (2014) 71–78, https://doi.org/10.1007/s12274-013-0372-0.
[59] C. Costentin, J.-M. Saveant, Cyclic voltammetry analysis of electrocatalytic films, J. Phys. Chem. C 119 (2015) 12174–12182, https://doi.org/10.1021/acs.jpcc.5b02376.
[60] L. Xiao, G.G. Wildgoose, R.G. Compton, Exploring the origins of the apparent "electrocatalysis" observed at C60 film-modified electrodes, Sens. Actuators B Chem. 138 (2009) 524–531, https://doi.org/10.1016/j.snb.2009.02.006.
[61] K.R. Ward, R.G. Compton, Quantifying the apparent 'Catalytic' effect of porous electrode surfaces, J. Electroanal. Chem. 724 (2014) 43–47, https://doi.org/10.1016/j.jelechem.2014.04.009.
[62] E.O. Barnes, X. Chen, P. Li, R.G. Compton, Voltammetry at porous electrodes: a theoretical study, J. Electroanal. Chem. 720–721 (2014) 92–100, https://doi.org/10.1016/j.jelechem.2014.03.028.
[63] A.V.N. Kumar, J. Joseph, New Zn–NiHCF hybrid electrochemically formed on glassy carbon: observation of thin layer diffusion during electro-oxidation of hydrazine, J. Phys. Chem. C 119 (2015) 296–304, https://doi.org/10.1021/jp508740w.
[64] J. Crank, The Mathematics of Diffusion, CLARENDON PRESS OXFORD, 1975.
[65] T. Pauporté, R. Durand, Impedance spectroscopy study of electrochromism in sputtered iridium oxide films, J. Appl. Electrochem. 30 (2000) 35–41, https://doi.org/10.1023/A:1003869328017.
[66] E. Barsoukov, J.R. Macdonald, Impedance spectroscopy: theory, experiment, and applications, 2005. doi:10.1002/0471716243.
[67] S.H. Glarum, J.H. Marshall, The A-C response of iridium oxide films, J. Electrochem. Soc. 127 (1980) 1467–1474, https://doi.org/10.1149/1.2129932.
[68] J. Backholm, A. Azens, G.A. Niklasson, Electrochemical and optical properties of sputter deposited Ir-Ta and Ir oxide thin films, Sol. Energy Mater. Sol. Cells 90 (2006) 414–421, https://doi.org/10.1016/j.solmat.2005.04.030.
[69] J. Backholm, P. Georń, G.a. Niklasson, Determination of solid phase chemical diffusion coefficient and density of states by electrochemical methods: Application to iridium oxide-based thin films, J. Appl. Phys. (2008) 103, https://doi.org/10.1063/1.2831484.